Supplemental Data

Nuclear Trapping Shapes the Terminal Gradient in the *Drosophila* Embryo

Mathieu Coppey, Alistair N. Boettiger, Alexander M. Berezhkovskii, and Stanislav Y. Shvartsman

Supplemental Experimental Procedures

Fly Strains and Whole-Mount Immunostaining

We used *OreR* and *histone-GFP* flies (a gift from E. Wieschaus) for wild-type experiments; $shkl^{GM130}/shkl^{GM73}$ and $Dp(1;Y)B^{S}$; ru^{1} gnu^{305} th^{1} st^{1} kni^{ri-1} rn^{roe-1} p^{p} e^{s} ca^{1}/TM3, Sb^{1} flies [S1, S2] for producing embryos with defects in nuclear density; tor^{XR1} heterozygous flies for *torso* partial deletion [S3, S4]; and tor^{R13I} for extra copies of *torso* (homozygous on the 2nd chromosome, transgene contains 13 kB *torso* genomic region, a gift from Willis Li). All flies were raised at 25°C; embryo collections were done at the same temperature. dpERK immunostaining was performed as described in [S5]. Embryos were dechorionated in 100% bleach for 1–2 min and rapidly transferred into 8 ml of fixing solution (4 ml, 8% formaldehyde in PBS and 4 ml of heptane). Embryos were then fixed for 25 min by gentle shaking on a nutator and were devitellinized by vigorous 1 min shaking in a mixture of heptane and methanol. Next, embryos were quickly rehydrated and transferred to the blocking and antibody steps of the protocol. All further processing was done with 0.2% PBS-Triton X-100 as the diluting solution. To mark the phosphorylated form of ERK, we used preabsorbed mouse monoclonal anti-dpERK antibody (Sigma; 1:100 dilution) and preabsorbed goat anti-mouse Alexa-546 secondary antibody (Molecular Probes; 1:500 dilution). When needed, nuclei were marked either with Hoescht (Molecular Probes; 1:10,000 dilution) or SYTOX Green (Invitrogen; 1:10,000 dilution), which were added to the secondary antibody solution for 10 min. Nonphosphorylated form of ERK was marked with preabsorbed mouse monoclonal anti-MAP Kinase, nonphosphorylated ERK antibody (Sigma; 1:100 dilution), and preabsorbed goat anti-mouse Alexa-546 secondary antibody (Molecular Probes; 1:500 dilution).

Image Processing

Confocal Microscopy

Imaging was done on a Zeiss LSM510 confocal microscope, with a Zeiss 20× (NA 0.45) A-plan objective. This produced high-resolution images (512 × 512 pixels 16 bits depth) from the focal plane either in the middle (for the dpERK gradient) or at the top (for counting the nuclei) of the embryo. Images of individual embryos were automatically extracted from raw confocal images and reoriented for gradient quantification, as described in the following section.

Image Preprocessing and Gradient Extraction

Images of individual embryos were extracted from confocal raw data by a custom-designed tool written in Matlab (R2006a) (see Figure S1). The script detects objects based on intensity, extracts the central embryo while removing extraneous objects, and reorients the image. Another image-processing tool was developed to extract the gradients from preprocessed images (see Figure S2). The script finds the perimeter of the embryo and then averages the staining intensity across a line normal to the boundary, until the signal drops to twice the value of the background. This was done for 1000 points uniformly spaced around the perimeter of the embryo, generating the quantified dpERK profile along the arc length of the boundary.

Determining Embryo Age

A third tool was developed to count the nuclei within a region of approximately 70 × 200 microns (see Figure S3). The nuclei were identified through a series of transformations, which equalize the intensity across the image, identify nuclei-sized objects, and separate connected nuclei before counting. Nuclear counts from multiple embryos were used to construct a cumulative distribution function (see Figure 3B).

Estimating the dpERK Nucleocytoplasmic Ratio

Confocal Microscopy and Image Processing

In these experiments, the histone-GFP embryos were used for imaging the dpERK gradient. We imaged only nuclear cycle 13 and 14 embryos. For younger embryos, the lower numbers and less regular arrangements of nuclei make the extraction of nuclear gradients less reliable. We extended the previous GUI to quantify at the same time the nuclear and cytoplasmic gradients. First, based on the GFP signal, we constructed a binary nuclear mask (see Figure S4). The mask was then applied to the dpERK staining in order to produce the images of the cytoplasmic and nuclear dpERK signals.

Quantifying the Nuclear-to-Cytoplasmic Ratio

Quantification of nuclear gradients in cycle 14 is straightforward, because the nuclei form a spatially homogeneous layer under the cortex of the embryo. Consequently, the resulting nuclear gradient is a smooth function of the spatial coordinate. Quantifying the nuclear gradients in cycle 13 embryos is less straightforward. At this stage, nuclei are clearly separated and the resulting nuclear gradient is a spatially modulated function, which is zero between the nuclei. To smooth this function, we averaged it over a sliding window that contains multiple nuclei. The size of the averaging window has to be larger than the internuclear distance but smaller than the decay length of the gradient. We then fitted the nuclear gradient to a linear function of the cytoplasmic gradient (via a robust fit MATLAB algorithm). The slope of the linear fit gives a spatially averaged value of the N/C ratio. Figure 4E of the main text shows an illustration of the linear fit for two embryos, one in cycle 13 and the other in cycle 14. The error bars correspond to the dispersion of the N/C ratio for *one* embryo when moving through the different values of the gradient. Figure S5 characterizes the variability of the N/C ratio extracted from multiple embryos.

Normalization

Normalization and Rescaling of Gradients

We removed the experimental noise that affects the amplitude and background intensity in each profile by the methods developed by Gregor et al. [S6]. This method, based on a simple model of the mapping between concentration and fluorescent intensity, was validated by direct measurements of the profile and concentration of the Bicoid morphogen. In brief, for every age class, the method selects a scaling factor and a background level for each profile, such that the variability between any profile and the mean profile (of the same class) is minimized (see [S6] for details). The embryos are not entirely rotationally symmetric. Hence, the position of the peak in the extracted gradient depends on the angle at which any given embryo is oriented under the coverslip. This can introduce translations in the position of peaks in the extracted intensity curves. We corrected for these translations by introducing a corrective translation to all the curves in order to maximize the cross-correlation of profiles within a given nuclear density class.

Validation of the Normalization Procedure

To validate the normalization procedure, we demonstrated that it can recover a given profile from a collection of corrupted versions of the same profile. Corrupted profiles were generated by applying several disturbances on the original profile (a Gaussian shape): first we applied a high-frequency noise, second we shifted left or right the gradient of a random amount, third we arbitrarily dilated or contracted the amplitude, and fourth we introduced a random background value (see Figure S6). The normalization procedure was able to trace back the original profile within 6% error, proving the efficiency of the method.

Validation of the Nuclear Cycle Grouping

If we do not separate the embryos by age before normalizing, the variance of the normalized profiles is more than 40% (see Figure S7). When we group embryos in the appropriate age categories prior to normalization, the variance within a class is from less than 7% to 14% (see Figure S7). If embryos of different ages belonged to the same distribution, then reducing the number of samples when grouping embryos by age would have increased the variability instead of reducing it. The remarkable similarity of profiles between embryos in the same division cycle supports the hypothesis that the number of nuclei (rather than the absolute age of the embryo) is responsible for the observed gradient dynamics.

Variability of the dpERK Gradient

The variability of the quantified gradient reflects the combined effects of the following factors: (1) the intrinsic variability in the terminal-patterning system, (2) the variability associated with imaging and gradient extraction, and (3) the variability associated with the fixation and immunostaining processes.

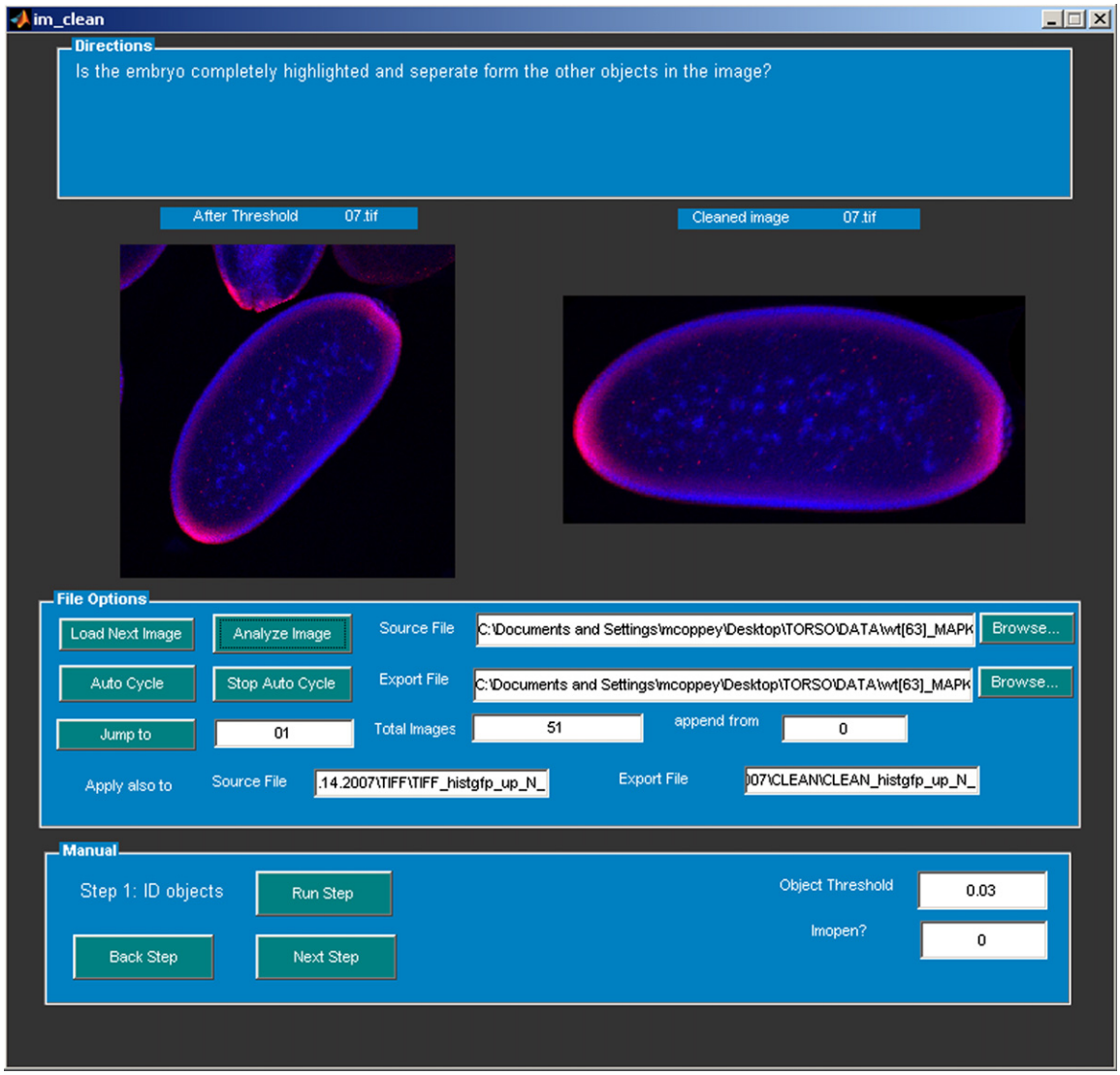

Figure S1. The Graphical User Interface Used to Remove Extraneous Objects from Image and Orient Embryos

Imaging and Image-Processing Variability

All embryos from a particular round of staining (typically, 30–60 embryos selected from a batch of stained embryos) were imaged during the same 2–4 hr confocal microscopy session. To quantify the variability associated with locating, focusing, and quantifying gradients from each embryo, we made repeated images of the same embryo, varying its orientation and location of the focal plane. These profiles were compared with the tools developed to compare distinct embryos. The extracted profiles from nine images of the same embryo are shown in Figure S9. Our normalization procedure can remove as much as 70% variability from this data set. The profiles differ between 5% and 10%, with an average deviation of 6%. This estimates the accuracy of our measurements.

Interembryo Image Variability

We investigated the experimental variability involved in imaging different embryos on the same slide, i.e., embryos that have been stained within an identical environment. We compared two groups of embryos stained simultaneously in a same tube. Both are of wild-type background, but one has the histone-GFP tag. All embryos in these data sets are in nuclear cycle 14. Because of experimental noise, the gradients from within each class of embryo differ considerably, similar to the observation for repeated imaging of the same embryo, with more significant total variations (see Figure S8). Our normalization procedure can remove a considerable amount of this variability (see Figure S8).

Interage Variability of dpERK Gradients

Focusing on a set of simultaneously fixed and stained embryos, we estimated the intrinsic variability of the dpERK gradient. Two main conclusions can be drawn from Figure S10, where the variability of each nuclear cycle group is plotted as a function of position. First, embryo-to-embryo variability in nuclear cycle 14, which equals 6.9% ± 0.08%, is close from the accuracy associated with imaging of a single embryo (6%, see above). Thus, the dpERK profile is surprisingly reproducible from embryo to embryo. In other words, profiles from 25 different embryos, spanning the range of orientations, varying in length (from 452 to 513 pixels), and potentially varying in their absolute age (between 2 and 3 hr, corresponding to the length of nuclear cycle 14) are essentially as similar as the profiles obtained from repetitive imaging of the same embryo. Second, the variability is time dependent: mean variability of nuclear cycle 10 gradients is ~14% ± 4%, whereas for cycle 14 embryos, it is ~6.9% ± 0.08%.

Mathematical Model

Consider a one-dimensional model of an embryo at a given nuclear density. dpERK is generated at rate Q at $x = 0$; this models the localized MAPK activation by the locally activated Torso receptors. The length scale of the dpERK gradient is much shorter than the size of the embryo, which allows us to model the embryo as semi-infinite in space. In our model, dpERK can be in two states: cytoplasmic, where it is moving

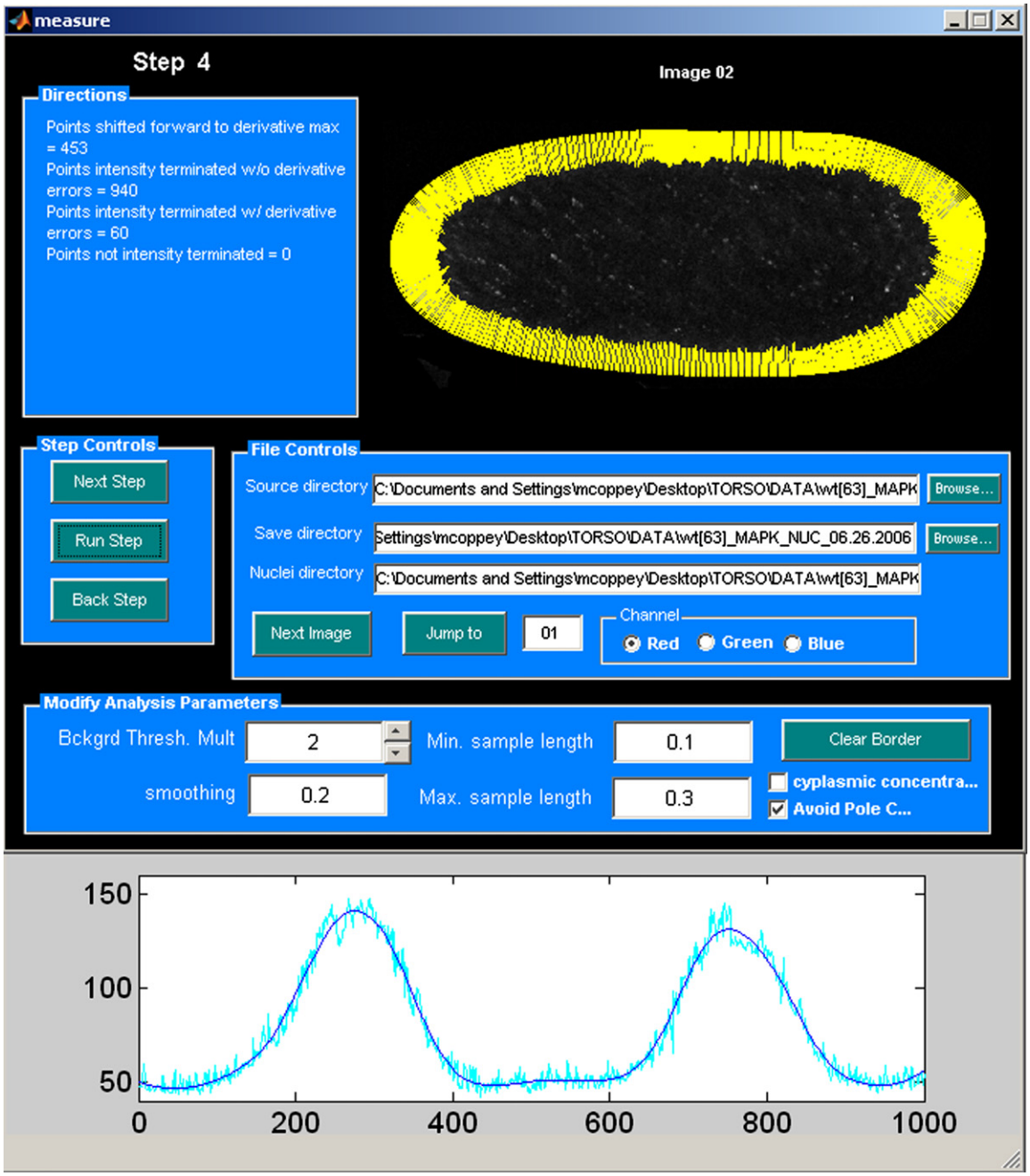

Figure S2. The GUI Used to Extract Quantitative Profiles of Morphogen Gradients

Once the file path and save path have been chosen, the GUI walks the user through a four-step procedure to quantify the MAPK gradient. The relevant analysis parameters can be modified in the bottom panel if desired. The yellow lines trace the rule-defined intervals over which the concentration is integrated.

with diffusivity D, and nuclear, where it is confined to the nucleus. The transitions between these two states are modeled by first-order processes with the rate constants k_+ and k_-, which model nuclear export and import. Finally, nuclear and cytoplasmic dpERK species are dephosphorylated with the first-order kinetics with rate constant k_c and k_n, respectively.

Low variability of the dpERK profiles within each nuclear cycle suggests that these profiles are in quasi steady state, which rapidly adjusts to the progressive increase in nuclear density. The concentrations of cytoplasmic and nuclear dpERK are denoted by $C_c = C_c(x)$ and $C_n = C_n(x)$, respectively. They are given by the following equations:

$$\frac{\partial C_c}{\partial t} = 0 = D\frac{\partial^2 C_c}{\partial x^2} - (k_+ + k_c)C_c + k_- C_n \quad (1)$$

$$\frac{\partial C_n}{\partial t} = 0 = k_+ C_c - (k_- + k_n)C_n \quad (2)$$

$$D\frac{\partial C_c}{\partial x}\Big|_{x=0} = -Q, C_c|_{x=\infty} = 0. \quad (3)$$

This simple model assumes that the unphosphorylated form of ERK is in excess and only cytoplasmic. This assumption is supported by the fact that

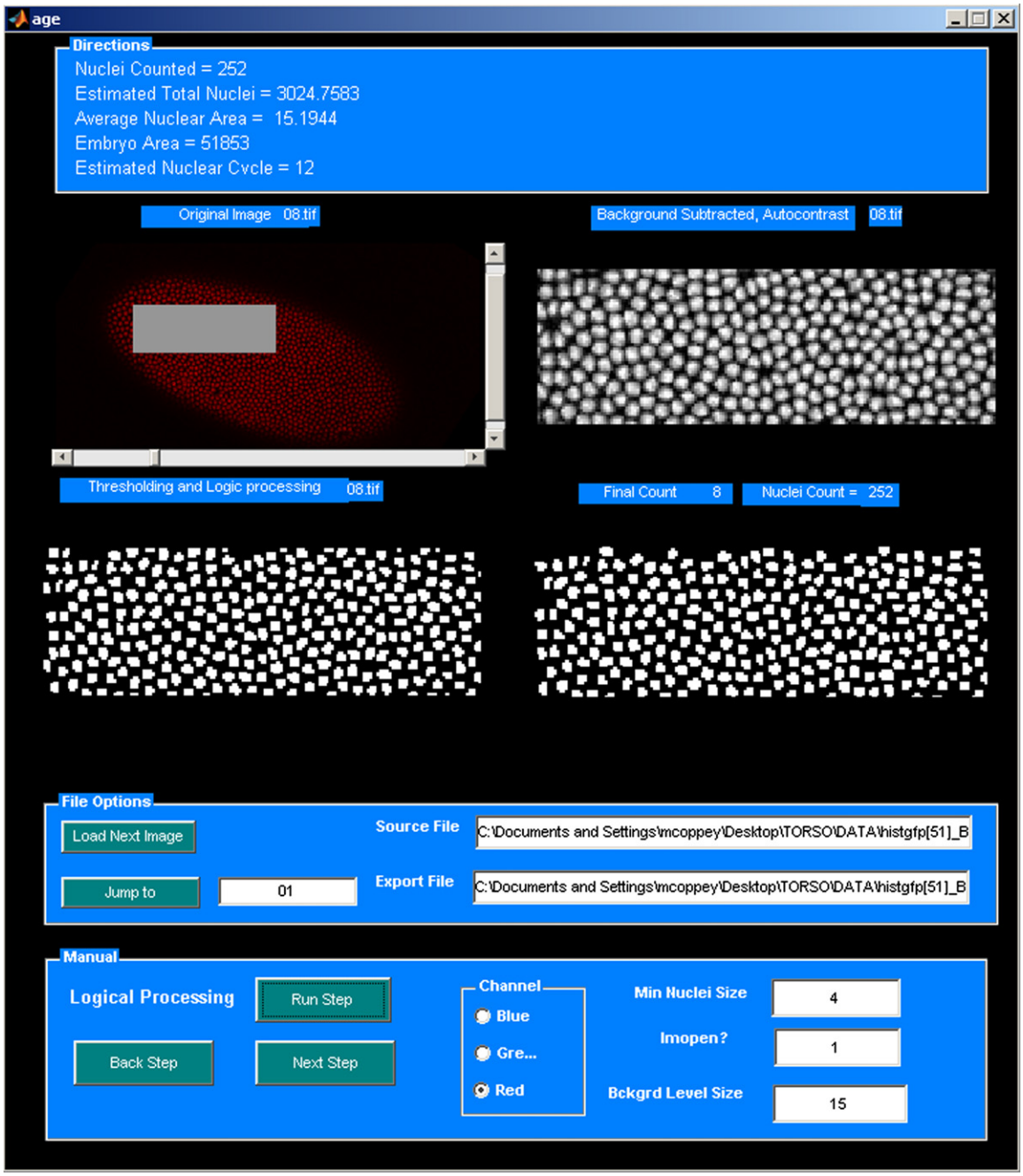

Figure S3. The GUI that Allows Easy Classification of the Embryo Age from Nuclear Density

The first screen shows the region of the embryo being used to calculate nuclear density. The user may navigate with the scroll arrows to a section where the nuclei are best resolved. The second screen shows the raw background-subtracted image, and the subsequent screens allow the user to compare the resolution achieved by three subsequent steps. The procedure is accurate enough to unambiguously place an embryo within the correct division cycle.

the pattern of unphosphorylated form of ERK is uniform throughout the embryo and predominantly cytoplasmic (Figure S11).

Our data reflect both the nuclear and cytoplasmic dpERK. In our model, this corresponds to the sum of the nuclear and cytoplasmic concentrations, denoted by $C_{tot}(x) = C_c(x) + C_n(x)$. With Equations (1)–(3), $C_{tot}(x)$ follows the system given by:

$$D\frac{d^2C_{tot}}{dx^2} - \left(k_c + \frac{k_n k_+}{k_- + k_n}\right)C_{tot} = 0 \qquad (4)$$

$$\frac{dC_{tot}}{dx}\Big|_{x=0} = -\frac{Q}{D}\left(1 + \frac{k_+}{k_- + k_n}\right), C_{tot}|_{x=\infty} = 0. \qquad (5)$$

The solution of this system reads:

$$C_{tot}(x) = Ae^{-\frac{x}{\lambda}}, \text{where } A \equiv \frac{Q(1 + k_+/(k_- + k_n))}{\sqrt{D(k_c + k_n k_+/(k_- + k_n))}}, \lambda \equiv \sqrt{\frac{D}{k_c + k_n k_+/(k_- + k_n)}} \qquad (6)$$

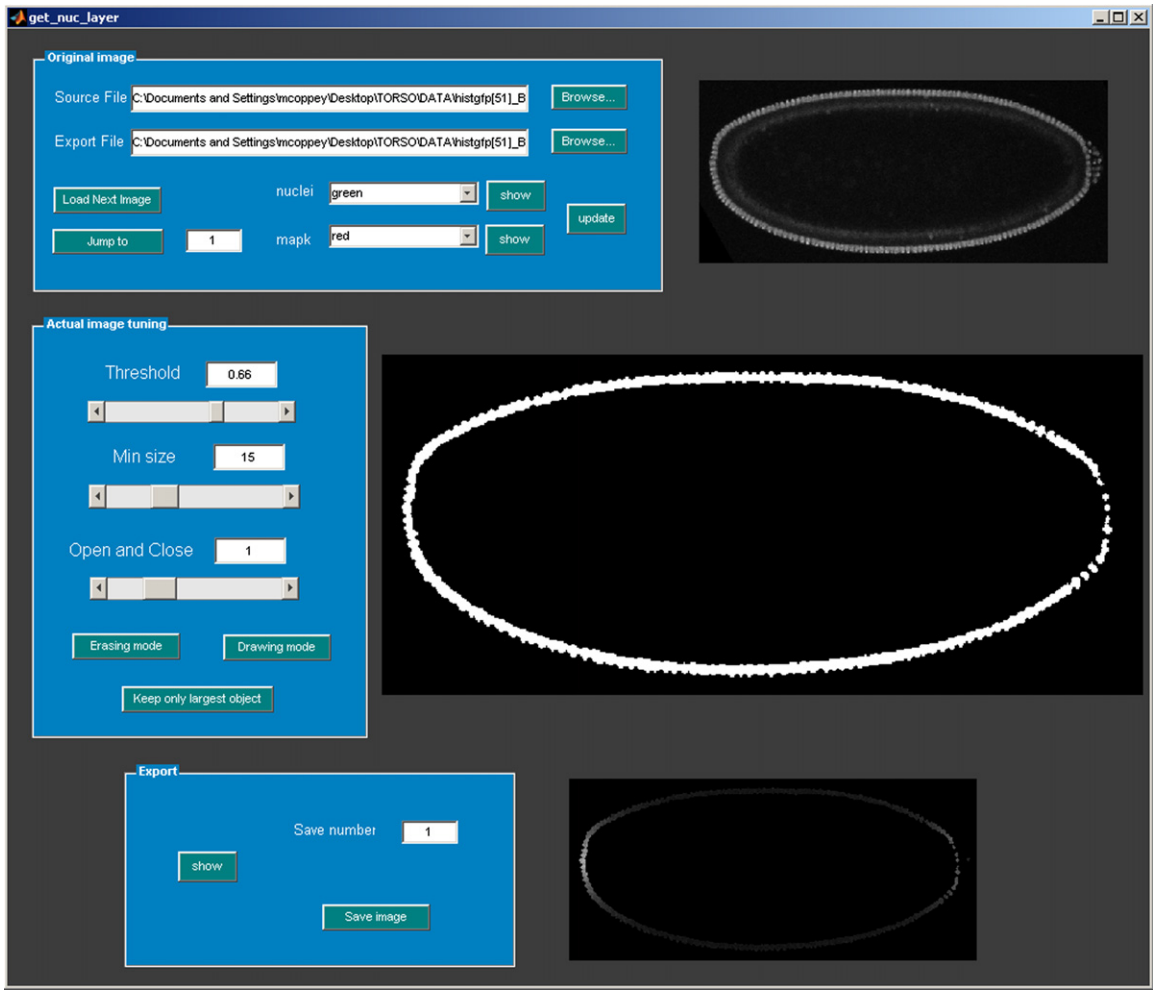

Figure S4. The GUI Developed in Order to Generate the Binary Mask Corresponding to the Nuclear Material

Thus, the spatial profile of the total dpERK is a decaying exponential function of distance from the source of the ligand. A and λ in Equation (6) are the amplitude of and the decay length of the signal, respectively. This expression allows us to analyze the effect of increasing nuclear density.

Analyzing the Effects of Nuclear Density

Qualitative agreement with the observed dynamics requires that C_{tot} is amplified close to the boundary and attenuated in the rest of the system. Within the framework of our model, a necessary condition for this behavior is that the amplitude of the signal (A) is an increasing function of nuclear density, whereas the decay length (λ) is a decreasing function of nuclear density. As we show below, this is indeed the case under not very restrictive assumptions.

Changes in the nuclear density affect the parameters in the model and, as a result, influence the amplitude and the decay length in Equation (6). To predict the effects of the nuclear density on A and λ, we need to specify how nuclear density influences the model parameters. We assume that the rate constants k_- and k_d, which characterize nuclear export of dpERK and its dephosphorylation in the nucleus, are not affected by changes in nuclear density. This is not unreasonable; they reflect the properties of a single nucleus and a single dpERK molecule.

On the other hand, the trapping rate constant (k_+), which depends both on the nuclear import rate constant and nuclear density, will increase with every nuclear division. The diffusivity is expected to be a decreasing function of nuclear density. This can be a consequence of several effects, e.g., the decreasing volume of the space available for diffusion between the nuclei. Finally, we assume that the rate of dpERK dephosphorylation in the cytoplasm does not depend on the nuclear density. This is the simplest assumption we can make at this point, when the precise identity of MAPK phosphatase in the syncytial embryo and its subcellular localization are unknown [S7].

To summarize, k_-, k_n, and k_c do not depend on the number of nuclei, whereas D and k_+ are decreasing and increasing functions of nuclear density, respectively. Under these assumptions, λ, the decay length of $C_{tot}(x)$, is always an increasing function of the nuclear density (Equation 6). Furthermore, one can show that an increase in the nuclear density will increase A, the amplitude of $C_{tot}(x)$, when $k_+/(k_n + k_-) > 1 - 2k_c/k_n$ (see below for the derivation). Thus, the necessary conditions required for gradient sharpening can be realized by a simple model based on diffusion and nucleocytoplasmic shuttling of dpERK.

The amplitude A in Equation (6) can be written as a product of $Q/\sqrt{D}$, which is an increasing function of nuclear density, and an expression that depends on nuclear density only through k_+. Because k_+ increases with nuclear density, a sufficient condition for the growth of A with nuclear density is given by:

$$\frac{d}{dk_+}\left(\frac{(1+k_+/(k_-+k_n))}{\sqrt{(k_c+k_nk_+/(k_-+k_n))}}\right)=\frac{1/(k_-+k_n)}{\sqrt{k_c+k_nk_+/(k_-+k_n)}}-\frac{k_n}{2(k_-+k_n)}\frac{1+k_+/(k_-+k_n)}{[k_c+k_nk_+/(k_-+k_n)]^{3/2}}>0. \quad (7)$$

This simplifies to:

$$\frac{k_+}{k_n+k_-}>1-\frac{2k_c}{k_n}. \quad (8)$$

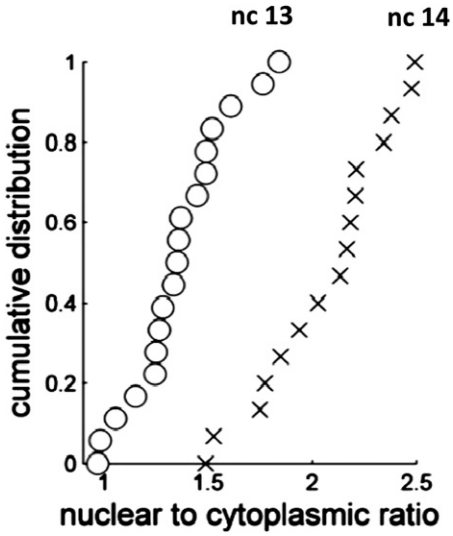

Figure S5. Cumulative Distribution of N/C Ratio

The mean N/C ratios are ~1.4 and ~2 in nuclear cycles 13 and 14, respectively (averaged over 19 and 17 embryos).

Thus, the necessary conditions required for gradient sharpening can be realized by a simple model based on diffusion and nucleocytoplasmic shuttling of dpERK. We analyzed then whether this result was robust with regards to more detailed modeling hypothesis. In particular, we analyzed the effect of the embryo geometry and the extension of the source by solving numerically the diffusion-trapping Equations (1)–(3) in prolate spheroidal coordinates. This system of coordinates provides a good approximation of the three-dimensional ellipsoid shape of the embryo [S8]. As seen in Figure S14, sharpening of the gradient is still occurring. The extended source (a Heaviside function) gives rise to a flattened peak, but away from the source, an exponential decay is observed as captured in our simplified 1d model. Note that the extended source reflects the extended distribution of *torso-like* proteins in the vitelline membrane as the diffusion-trapping module in the perivitelline space perfectly matches the source of *trunk* ligand production.

Supplemental References

S1. Yohn, C.B., Pusateri, L., Barbosa, V., and Lehmann, R. (2003). l(3)malignant brain tumor and three novel genes are required for *Drosophila* germ-cell formation. Genetics *165*, 1889–1900.

S2. Freeman, M., Nüsslein-Volhard, C., and Glover, D.M. (1986). The dissociation of nuclear and centrosomal division in gnu, a mutation causing giant nuclei in *Drosophila*. Cell *46*, 457–468.

S3. Cleghon, V., Gayko, U., Copeland, T.D., Perkins, L.A., Perrimon, N., and Morrison, D.K. (1996). *Drosophila* terminal structure development is regulated by the compensatory activities of positive and negative phosphotyrosine signaling sites on the Torso RTK. Genes Dev. *10*, 566–577.

S4. Schupbach, T., and Wieschaus, E. (1986). Maternal-effect mutations altering the anterior-posterior pattern of the *Drosophila* embryo. Rouxs Arch. Dev. Biol. *195*, 302–317.

S5. Gabay, L., Seger, R., and Shilo, B.Z. (1997). MAP kinase in situ activation atlas during *Drosophila* embryogenesis. Development *124*, 3535–3541.

S6. Gregor, T., Wieschaus, E., McGregor, A.P., Bialek, W., and Tank, D.W. (2007). Stability and nuclear dynamics of the Bicoid morphogen gradient. Cell *130*, 141–153.

S7. Kim, M., Cha, G.H., Kim, S., Lee, J.H., Park, J., Koh, H., Choi, K.Y., and Chung, J. (2004). MKP-3 has essential roles as a negative regulator of the Ras/mitogen-activated protein kinase pathway during *Drosophila* development. Mol. Cell. Biol. *24*, 573–583.

S8. Coppey, M., Berezhkovskii, A.M., Kim, Y., Boettiger, A.N., and Shvartsman, S.Y. (2007). Modeling the Bicoid gradient: diffusion and reversible nuclear trapping of a stable protein. Dev. Biol. *312*, 623–630.

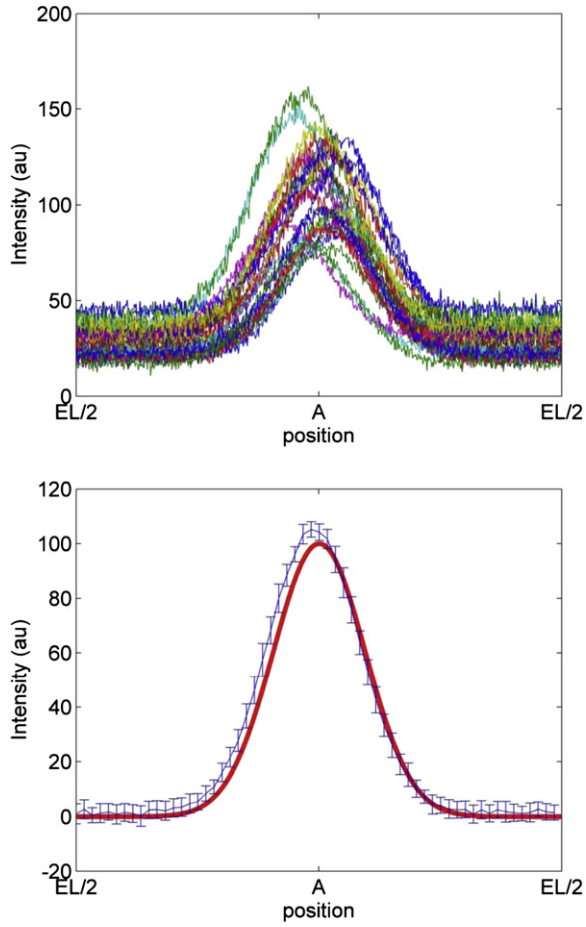

Figure S6. Validation of the Normalization Procedure

Artificial gradients (top) created by corrupting an arbitrary source gradient (red trace, bottom plot) can be used to reconstruct the original source gradient with high accuracy (blue data, bottom plot). Error bars are obtained from the standard deviation of the normalized profiles calculated for different positions along the spatial coordinate.

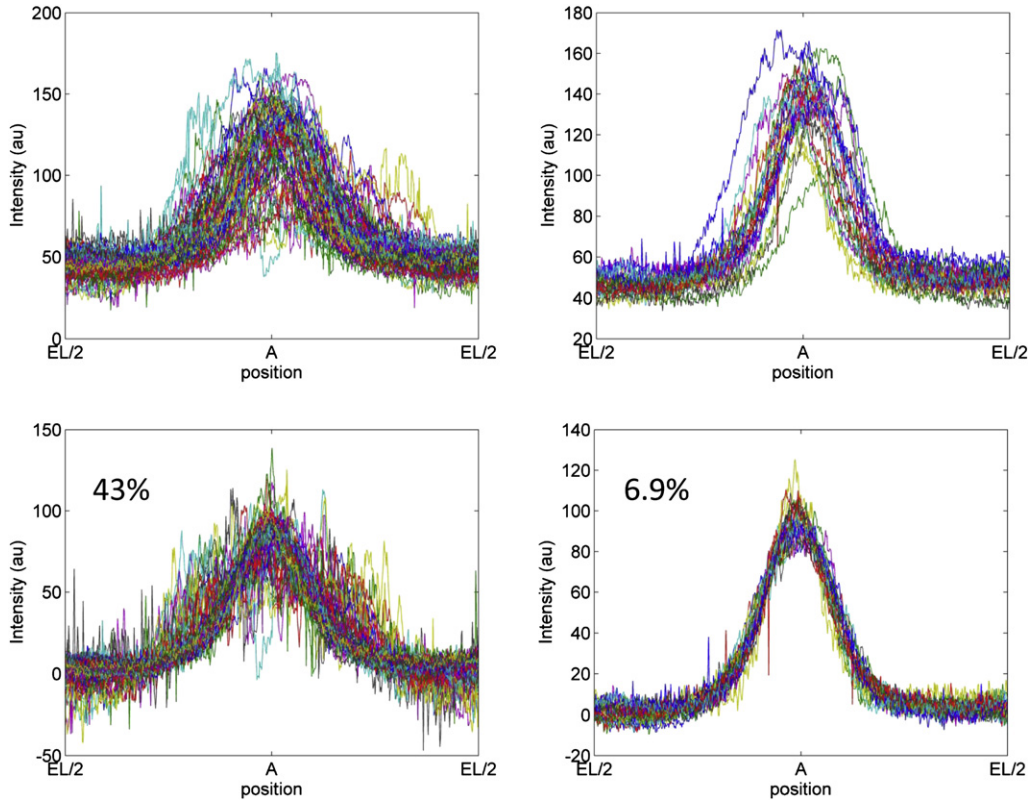

Figure S7. Normalization of dpERK Gradient in One Batch or Separating Age Groups

Left: without separating the embryos by age class before normalization, the profiles cannot be superimposed. The average variability from the mean is more than 40%. Right: separating embryos by age allows the profiles to be neatly superimposed. The variability among these nuclear cycle 14 embryos is essentially the same as the variability in duplicate photos of the same embryo.

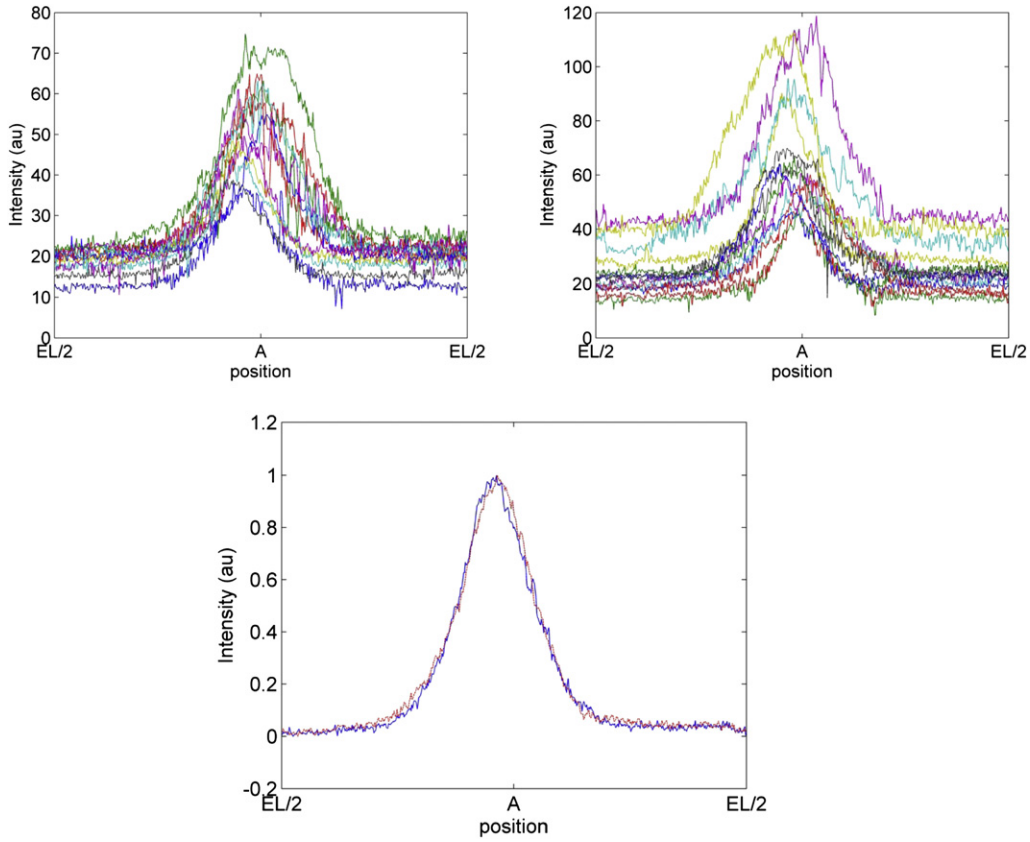

Figure S8. Interembryo Variability in Imaging

Because of experimental noise, the gradients from within each class of embryo differ considerably. Top left, raw data from OreR flies; top right, raw data from histone-GFP-labeled wild-type flies. Bottom: if we filter each set of profiles by using the normalization procedure described, the average profiles from each group superimpose almost perfectly.

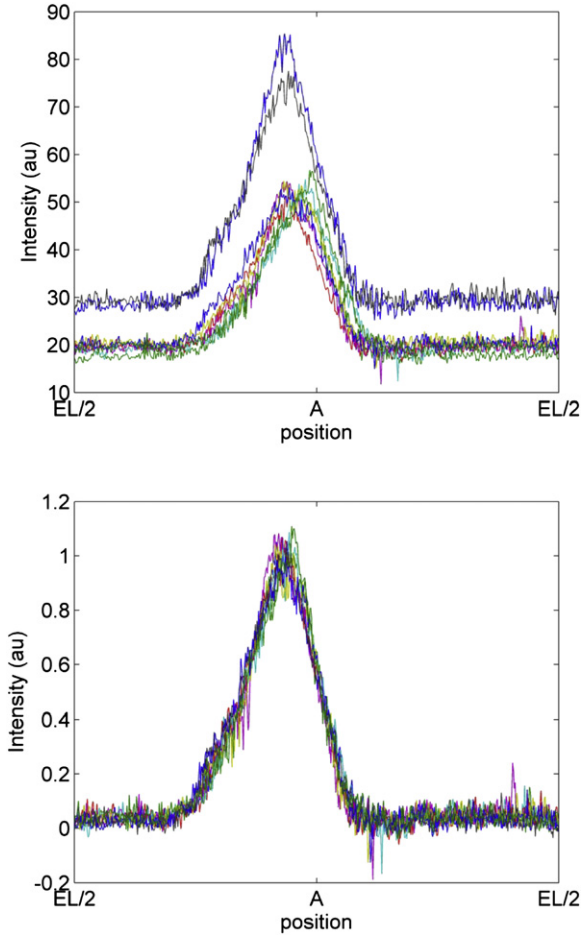

Figure S9. Variability of the Image Processing Time

Top: nine unscaled anterior profiles from the same embryo. Bottom: rescaled profiles to filter experimental noise collapse neatly onto one another. The remaining 5%–10% variations provides an indication of the precision limit of our procedures. The average variance is only 6%.

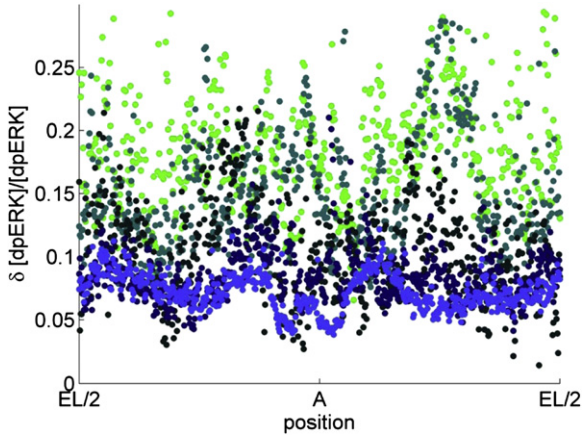

Figure S10. Embryo-to-Embryo Variability of MAPK Profiles from the Set of 63 Embryos Treated Simultaneously

The variability is plotted as a function of space for the five distinct age classes (light green nc 10 to light blue nc 14). Averaged over space variability is: 14% ± 4% for nuclear cycle 10, 14% ± 1% for nuclear cycle 11, 10% ± 0.4% for nuclear cycle 12, 9.1% ± 0.2% for nuclear cycle 13, 6.9% ± 0.08% for nuclear cycle 14.

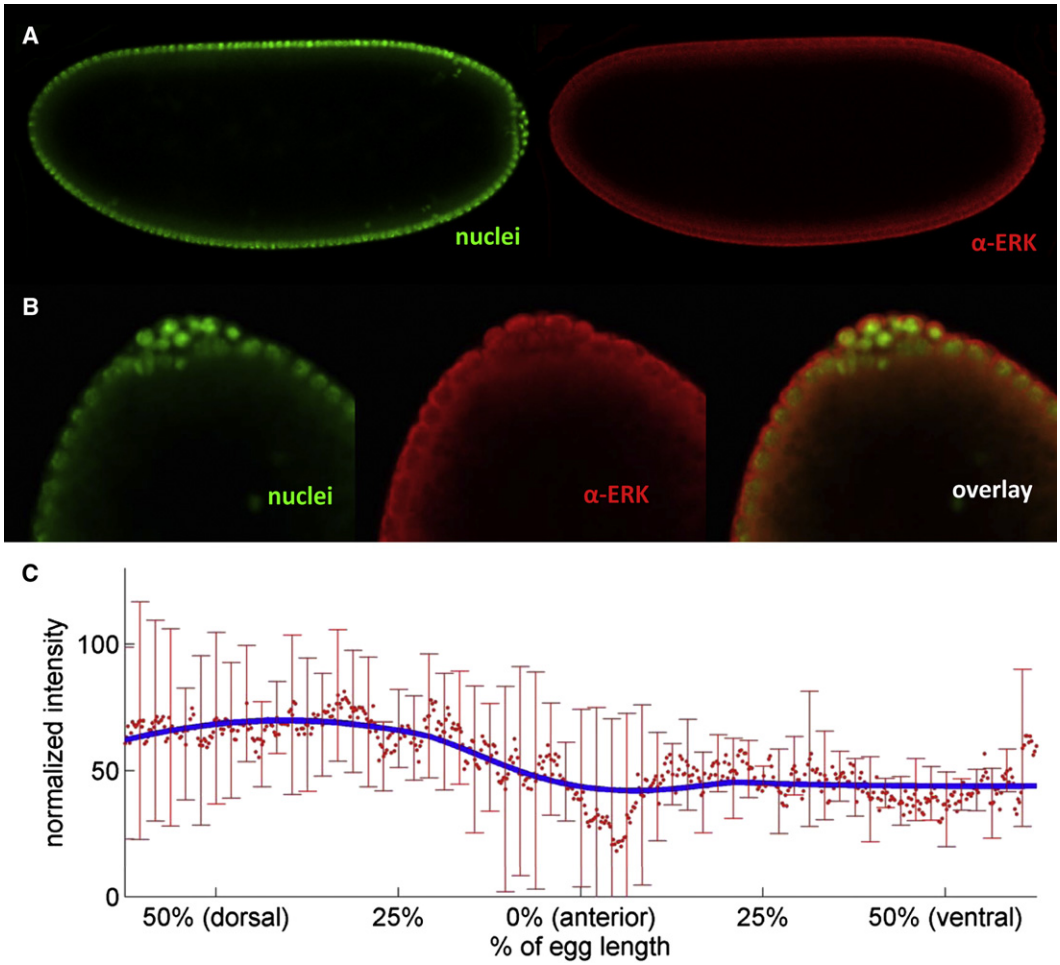

Figure S11. Wild-Type Embryo in Nuclear Cycle 13 Stained with the Antibody Recognizing the Unphosphorylated Form of ERK

(A) The distribution of unphosphorylated ERK appears uniform all around the embryo.

(B) A closer look to the posterior pole of the embryo shows that unphosphorylated ERK is mostly cytoplasmic and mainly localized in the thin cytoplasmic cortex between the cytoplasmic membrane and the nuclear layer.

(C) The quantified spatial distribution of unphosphorylated ERK (averaged over five embryos) shows an almost flat distribution with a slight dip at the anterior tip. Thus unphosphorylated ERK and therefore total ERK are in excess in comparison to dpERK. The spatial coordinate of the plot ranges from the most dorsal point to the most ventral point passing through the anterior tip. Error bars are obtained from the standard deviation of the normalized profiles calculated for different positions along the spatial coordinate.

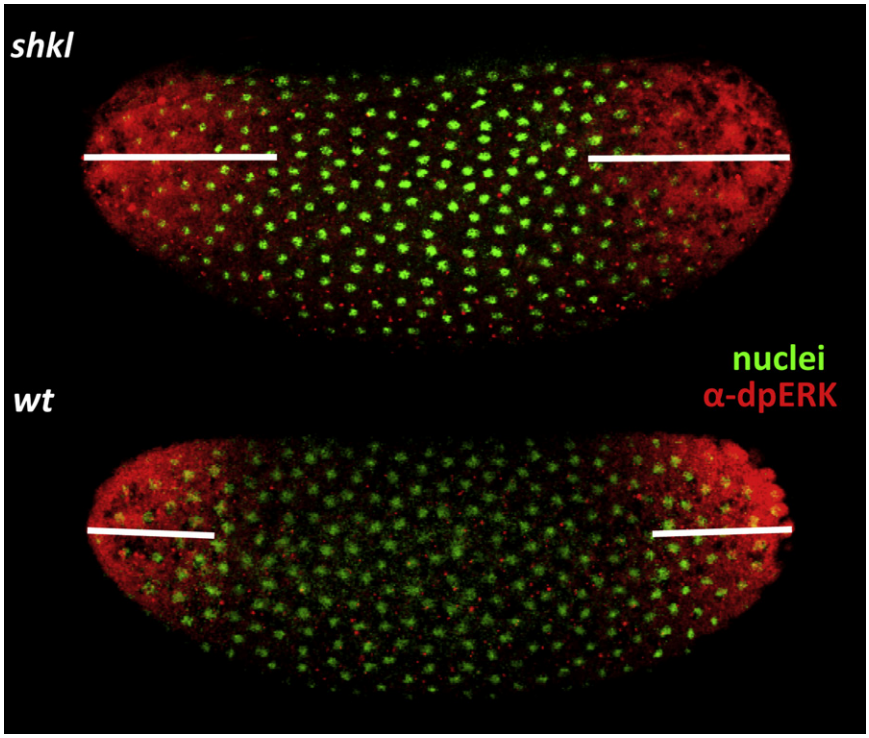

Figure S12. dpERK Patterns in the Early *shkl* Embryo

The dpERK profile appears more extended than the wild-type profile of the same nuclear cycle. For this early nuclear cycle, *shkl* mutant exhibits a delay in the migration of the nuclei at the poles of the embryo resulting in a depletion of nuclear material at these specific positions. The extension of the dpERK gradient might be a consequence of the nonautonomous role of nuclei.

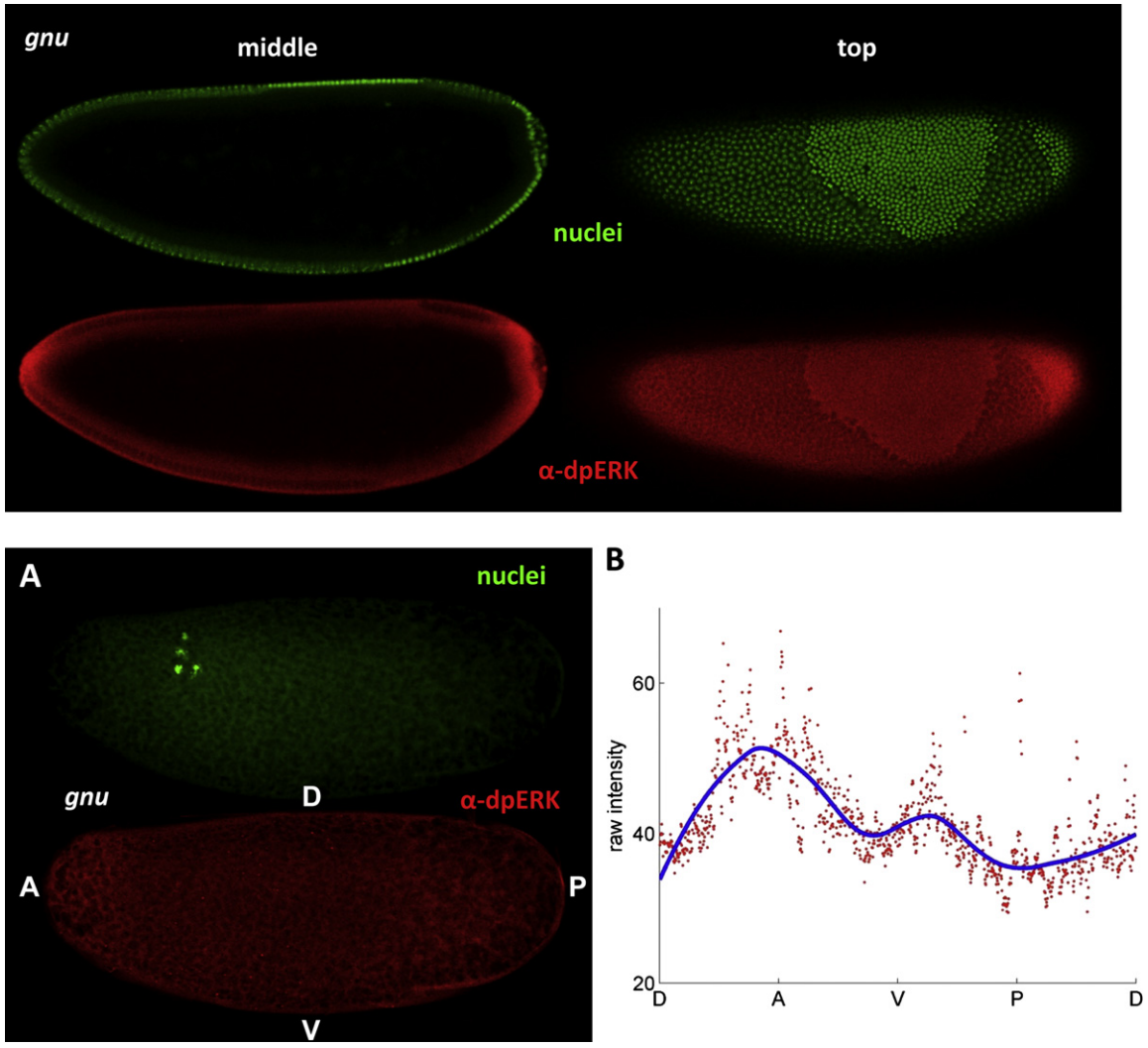

Figure S13. dpERK Patterns in *gnu* Embryos Show Clear Disruptions of the dpERK Gradient

Top images show an embryo showing a mixture of nuclear cycles 13 and 14 syncytial nuclei. The middle view shows that on top of the normal dpERK gradient, the signal appears brighter in regions for which nuclei are in cycle 14. This suggests that the dpERK concentration increases with nuclear concentration.

Bottom images are as follows.

(A) A characteristic *gnu* mutant embryo, showing few giant nuclei. The dpERK profile appears almost flat, suggesting that without the spatially uniform trapping by the nuclei, the dpERK molecules tend to distribute evenly. However, because the mutant phenotype makes impossible the determination of the embryo age, the dpERK profile seen in this particular embryo might be very early. We found that these observations hold for all the embryos having the characteristic mutant phenotype of *gnu* flies (few giant nuclei).

(B) The quantified dpERK spatial distribution all along the contour of the embryo shows that the posterior gradient is absent and that the anterior gradient is still present but much more extended and flattened than in wild-type embryos.

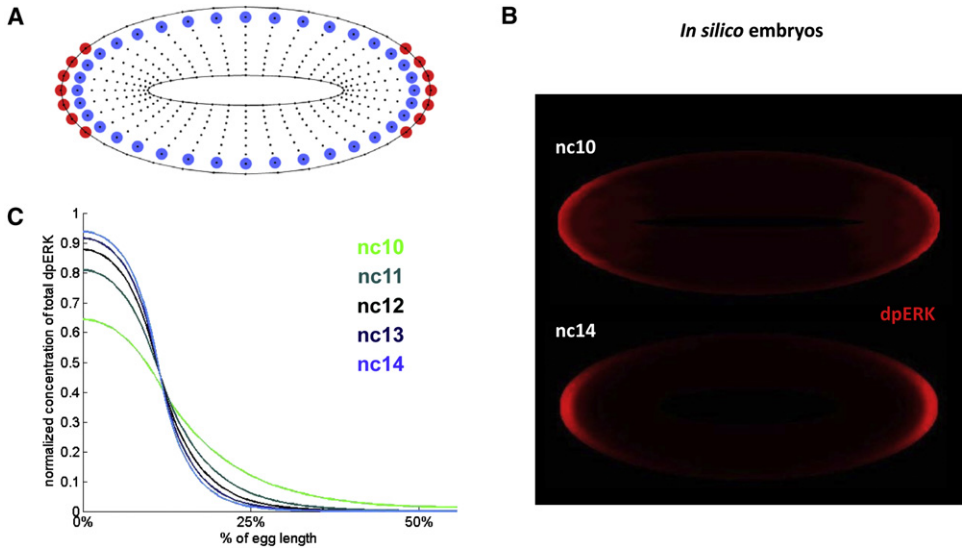

Figure S14. Diffusion-Trapping Model in Three Dimensions

(A) The prolate spheroidal mesh used for numerical simulations. Black dots are accessible spatial position for dpERK molecules, blue circles are nuclear traps, red circle are points of constant source production, and black lines are reflecting boundaries.

(B) Steady-state solutions of dpERK profiles for five increasing nuclear concentrations. dpERK concentration is averaged along the curves normal to the surface of the embryo. Sharpening occurs as in the simplified 1d model.

(C) Two-dimensional representations of early and late in silico embryos that correspond to the first and last curves plotted in (B).